

Figure S1. Related to Figure 1.

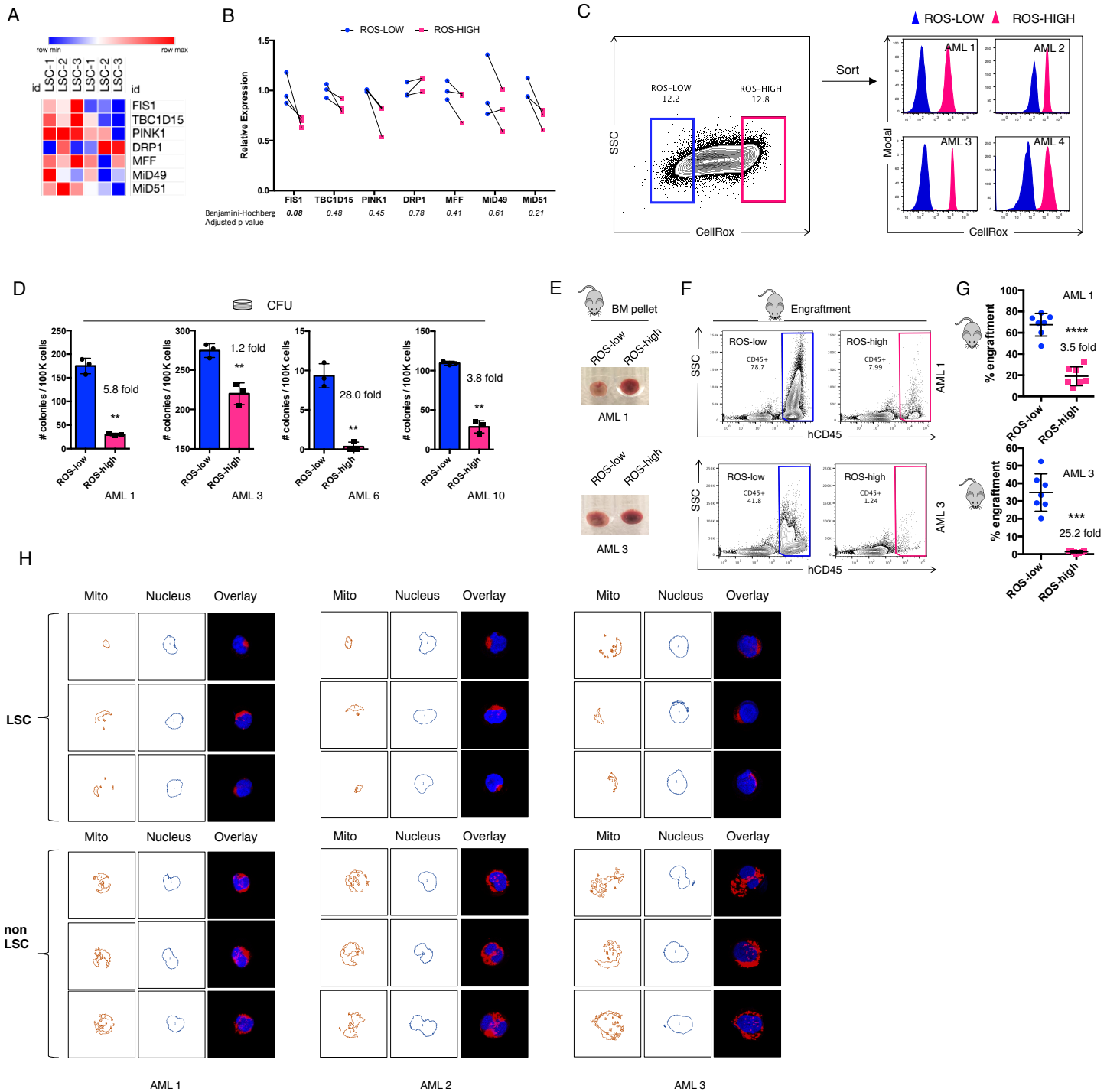


Figure S1. Related to Figure 1. Characterization of ROS-low LSCs and ROS-high non-LSCs from primary AML specimens

(A) A heat map showing expression of mitophagy and mito-fission genes in ROS-low LSCs versus ROS-high non-LSCs. 3 primary AML specimens are included in this study. **(B)** Relative expression of mitophagy and mito-fission genes in ROS-low LSCs versus ROS-high non-LSCs. Benjamini-Hochberg adjusted p-values of each comparison is listed at the bottom of the graph. 3 primary AML specimens are included in this study. **(C)** Flow cytometry plots showing CellRox staining pattern of representative primary AMLs before sort and purity of ROS-low LSCs and ROS-high non-LSCs after sort. **(D)** Colony-forming potential of sorted ROS-low and ROS-high AML cells (n=3). 4 primary AML are evaluated. Fold change is labeled. Type 2, two-tailed t-test. ******p<0.01. **(E)** Representative Images of bone marrow pellets isolated from mice engrafted with ROS-low and ROS-high AML cells. Notice the pellet from ROS-low engrafted mice is distinctly paler than the pellet from ROS-high engrafted mice, suggesting more engraftment burden in them. **(F)** Representative flow cytometry plots showing tumor burden (% human CD45+) in ROS-low and ROS-high engrafted mice. **(G)** Percentage of engraftment identified in ROS-low and ROS-high engrafted mice. Each dot represents an individual mouse. Lines represent mean ± SD. Fold change is labeled. Type 2, two-tailed t-test. *******p<0.001, ********p<0.0001. **(H)** Representative images showing segregation of mitochondrial and nuclear channels from confocal images of LSCs and non-LSCs of primary AML 1, 2 and 3. For each condition, 3 representative images are shown. The areas of the separated channels were used to calculate mitochondrial to nuclear area ratio shown in Figure 1F.

Figure S2. Related to Figure 2.

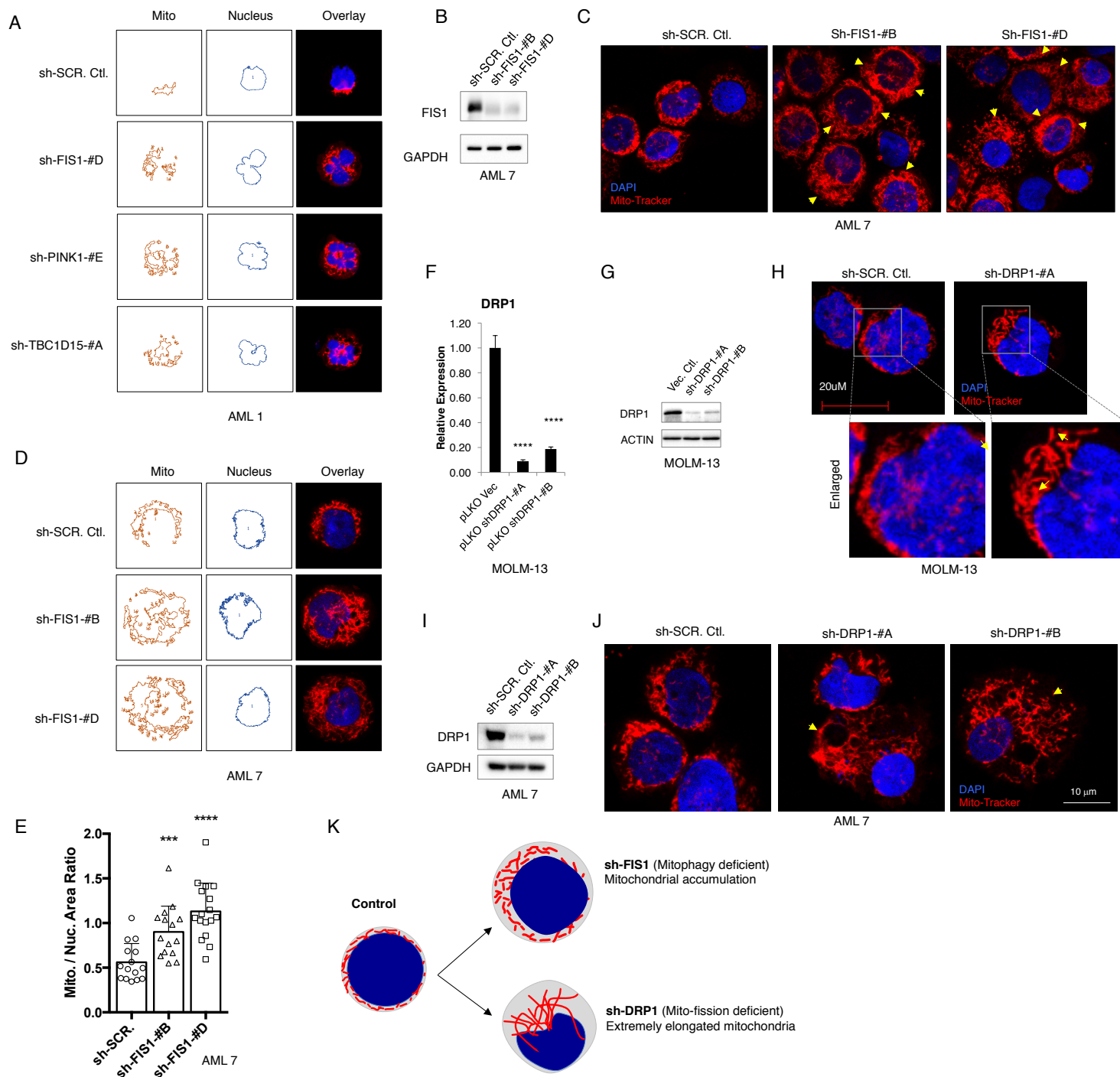


Figure S2. Related to Figure 2. Mitochondrial morphology of AML cells depleted with mitochondrial dynamics regulators

(A) Representative images showing segregation of mitochondrial and nuclear channels from confocal images of AML 1 with different knock-downs. The areas of the separated channels were used to calculate mitochondrial to nuclear area ratio shown in Figure 2G. (B) WB results showing knock-down efficiency of shFIS1 in AML 7. (C) Representative confocal images showing mitochondrial morphology of primary AML 7 at day 6 following shRNA-mediated knock-down of FIS1. Arrows highlight mitochondrial accumulation. (D) Representative images showing segregation of mitochondrial and nuclear channels from confocal images of AML 7 with FIS1 knock-down. The areas of the separated channels were used to calculate mitochondrial to nuclear area ratio shown in Figure S2E. (E) Quantification results showing mitochondrial to nuclear area ratio in AML 7 with or without FIS1 knock-down. For each condition, ~30-60 cells from 3 or more fields were quantified in ImageJ. Each dot represents an individual cell. Type 3, two-tailed t-test. *** $p < 0.001$, **** $p < 0.0001$. (F) qPCR results showing knock-down efficiency of shDRP1 in MOLM-13 cells. Type 2, two-tailed t-test. **** $p < 0.0001$. (G) WB results showing knock-down efficiency of shDRP1 in MOLM-13 cells. (H) Representative confocal images showing mitochondrial morphology of MOLM-13 cells at day 6 following shRNA-mediated knock-down of DRP1. Inserts show enlarged view of mitochondrial network. Arrows highlight extensively elongated mitochondria in shDRP1 cells. (I) WB results showing knock-down efficiency of shDRP1 in primary AML 7. (J) Representative confocal images showing mitochondrial morphology of primary AML cells at day 6 following shRNA-mediated knock-down of DRP1. Arrows highlight extensively elongated mitochondria in shDRP1 cells. (K) A diagram summarizing differences in mitochondrial accumulation and elongation phenotypes induced by shFIS1 and shDRP1, respectively.

Figure S3. Related to Figure 3.

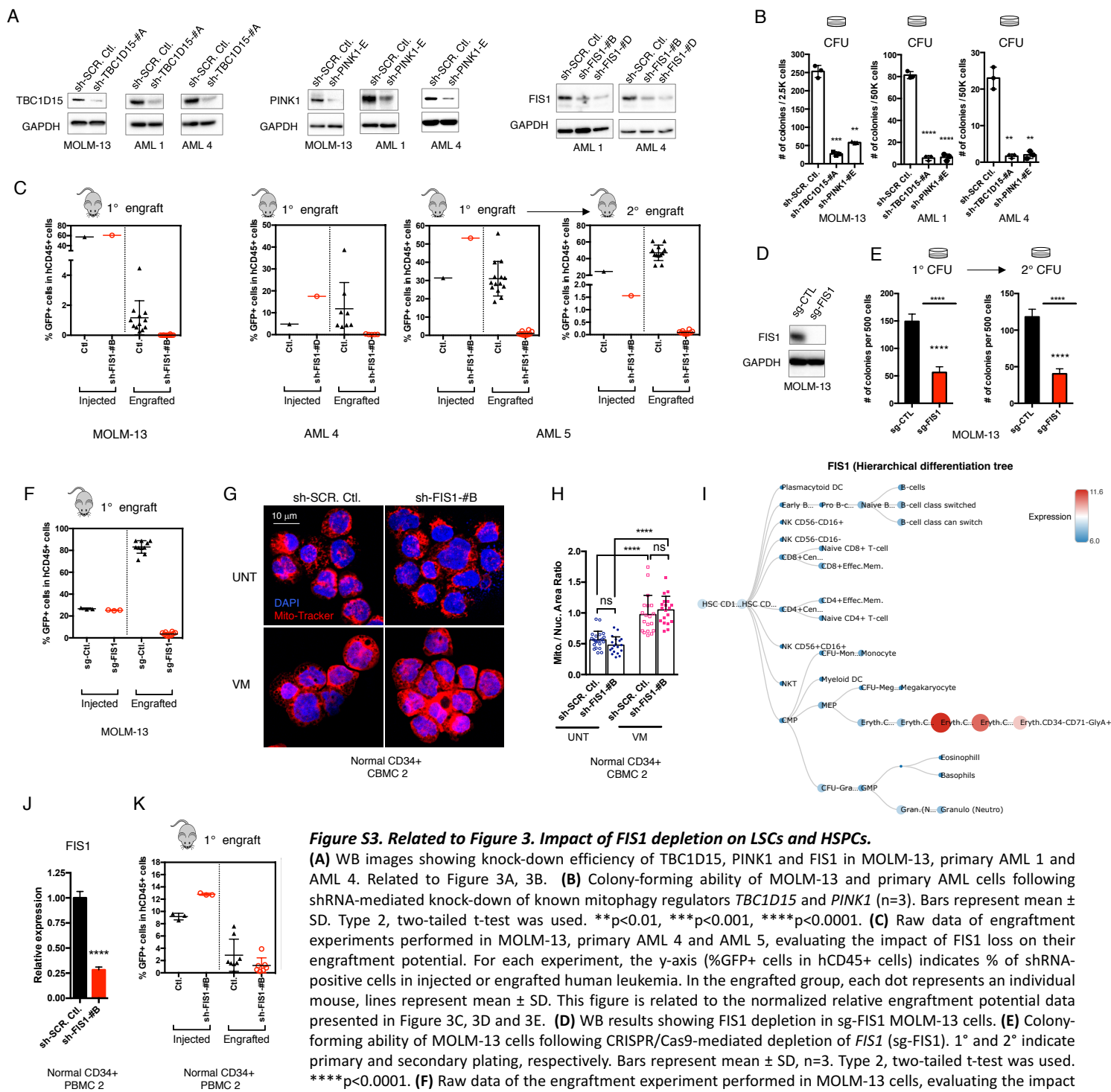


Figure S3. Related to Figure 3. Impact of FIS1 depletion on LSCs and HSPCs.

(A) WB images showing knock-down efficiency of TBC1D15, PINK1 and FIS1 in MOLM-13, primary AML 1 and AML 4. Related to Figure 3A, 3B. (B) Colony-forming ability of MOLM-13 and primary AML cells following shRNA-mediated knock-down of known mitophagy regulators *TBC1D15* and *PINK1* ($n=3$). Bars represent mean \pm SD. Type 2, two-tailed t-test was used. $**p<0.01$, $***p<0.001$, $****p<0.0001$. (C) Raw data of engraftment experiments performed in MOLM-13, primary AML 4 and AML 5, evaluating the impact of FIS1 loss on their engraftment potential. For each experiment, the y-axis (%GFP+ cells in hCD45+ cells) indicates % of shRNA-positive cells in injected or engrafted human leukemia. In the engrafted group, each dot represents an individual mouse, lines represent mean \pm SD. This figure is related to the normalized relative engraftment potential data presented in Figure 3C, 3D and 3E. (D) WB results showing FIS1 depletion in sg-FIS1 MOLM-13 cells. (E) Colony-forming ability of MOLM-13 cells following CRISPR/Cas9-mediated depletion of *FIS1* (sg-FIS1). 1° and 2° indicate primary and secondary plating, respectively. Bars represent mean \pm SD, $n=3$. Type 2, two-tailed t-test was used. $****p<0.0001$. (F) Raw data of the engraftment experiment performed in MOLM-13 cells, evaluating the impact of sg-FIS1 on their engraftment potential. The y-axis (%GFP+ cells in hCD45+ cells) indicates % of sg-control or sg-FIS1 cells in injected or engrafted MOLM-13 cells. In the engrafted group, each dot represents an individual mouse, lines represent mean \pm SD. (G) Representative confocal images showing mitochondrial morphology in control or FIS1 knock-down normal CD34+ CBMCs with or without 3 hours of 5uM valinomycin treatment. (H) Quantification results showing mitochondrial to nuclear area ratio in control or shFIS1 normal CD34+ CBMCs with or without 3 hours of 5uM valinomycin treatment. For each condition, ~30-60 cells from 3 or more fields were quantified. Each dot represents an individual cell. Bars represent mean \pm SD. Type 3, two-tailed t-test. $****p<0.0001$. ns indicates not significant. (I) A graph generated from the BloodSpot website showing color coded relative expression of *FIS1* gene during human hematopoietic differentiation. Raw data is published by Novershtern et al. (GSE24759). (J) qPCR results showing knock-down efficiency of shFIS1 in normal CD34+ PBMCs. Type 2, two-tailed t-test. $****p<0.0001$. (K) Raw data of the engraftment experiment performed in normal CD34+ PBMCs, evaluating the impact of FIS1 loss on their engraftment potential. The y-axis (%GFP+ cells in hCD45+ cells) indicates % of shRNA-positive cells in injected or engrafted human cells. In the engrafted group, each dot represents an individual mouse, lines represent mean \pm SD. This figure is related to the normalized relative engraftment potential data presented in Figure 3I.

Figure S4. Related to Figure 4.

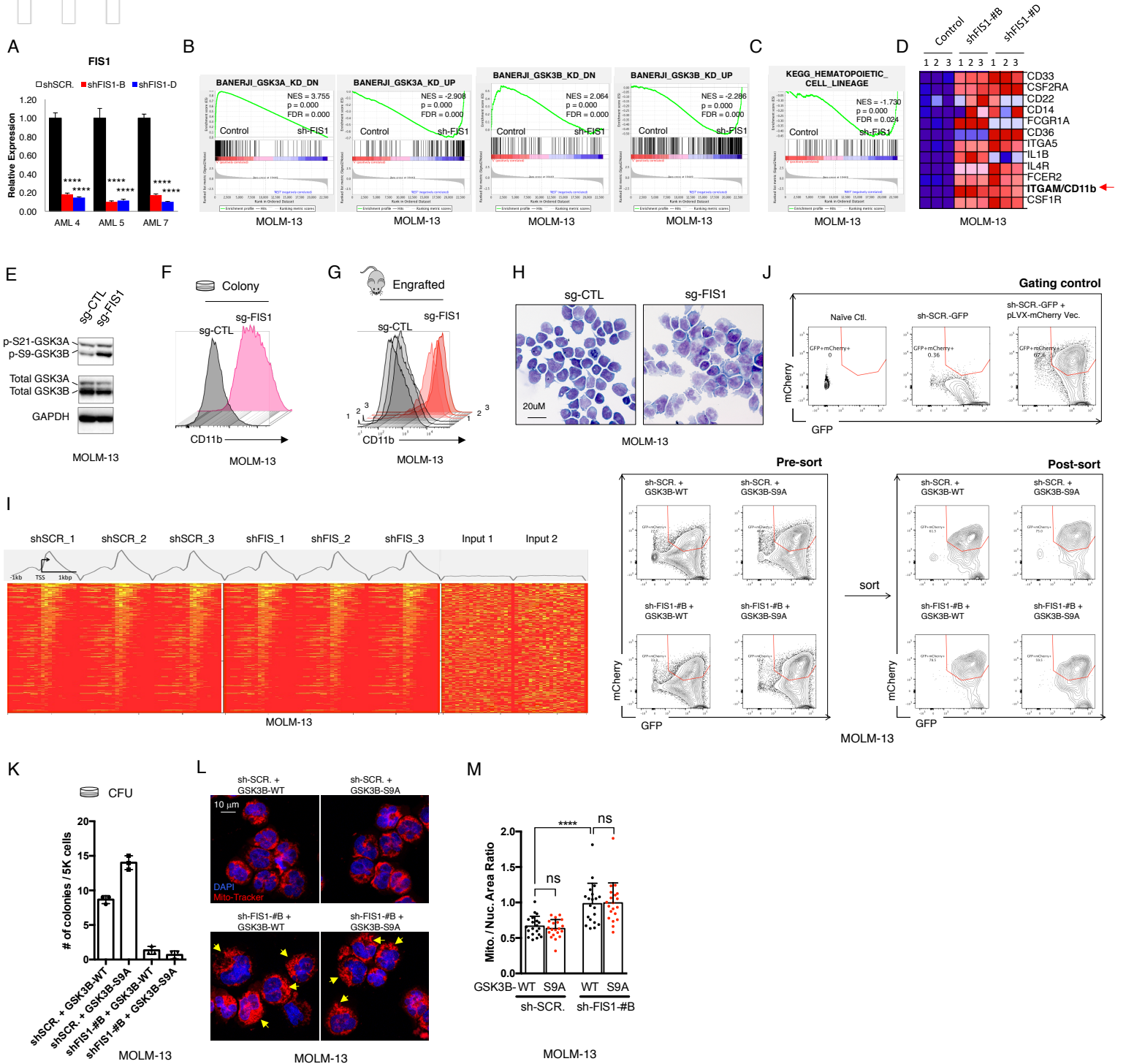
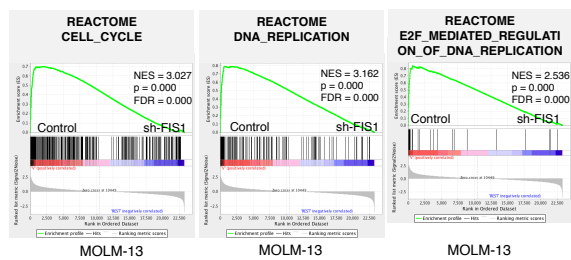


Figure S4. Related to Figure 4. Loss of FIS1 induces GSK3 inactivation and myeloid differentiation

(A) qPCR results showing significant knock-down efficiency of shFIS1 in primary AML 4, 5 and 7, used for the RNA-seq experiment. (B) GSEA enrichment plots showing loss of FIS1 in MOLM-13 cells (3 technical replicates) results in enrichment of several GSK3-related gene sets produced by Banerji et al. “sh-FIS1” represents sh-FIS1-#B and sh-FIS1-#D together. (C) A GSEA enrichment plot showing loss of FIS1 in MOLM-13 cells (3 technical replicates) results in significant up-regulation of the KEGG_HEMATOPOIETIC_CELL_LINEAGE gene set. “sh-FIS1” represents sh-FIS1-#B and sh-FIS1-#D together. (D) A heat map showing expression of representative hematopoietic lineage related genes in control versus sh-FIS1 MOLM-13 cells. (E) WB images showing expression of p-S21-GSK3A, p-S9-GSK3B, total GSK3A and total GSK3B in sg-CTL and sg-FIS1 MOLM-13 cells. GAPDH is used as loading control. (F) Histograms showing expression of CD11b in sg-CTL versus sg-FIS1 cells isolated from colonies grown in methylcellulose. (G) Histograms showing expression of CD11b in sg-CTL versus sg-FIS1 cells isolated from engraftment in NSGS mice. (H) Giemsa staining images showing morphology of sg-CTL versus sg-FIS1 MOLM-13 cells. Arrows highlight distinct morphology indicating differentiation. (I) Heat maps showing H3K27ac ChIP-seq signals at the promoter regions of top 2000 genes ranked by strength of overall H3K27ac ChIP signal in shSCR_1 (replicate 1). The heat map signals were normalized per gene within boundary colors (max=yellow, min=red). “TSS” stands for transcriptional starting sites. (J) Flow cytometry plots showing the gating strategy, pre-sort and post-sort purity of the double genetic rescue experiment. (K) Colony-forming ability of MOLM-13 cells expressing different combination of GSK3 alleles and shFIS1. (L) Representative confocal images showing mitochondrial morphology in MOLM-13 cells expressing different combination of GSK3 alleles and shFIS1. (M) Quantification results showing mitochondrial to nuclear area ratio in MOLM-13 cells expressing different combination of GSK3 alleles and shFIS1. For each condition, ~30-60 cells from 3 or more fields were quantified. Each dot represents an individual cell. Bars represent mean + SD. Type 3, two-tailed t-test. ****p<0.0001. ns indicates not significant.

Figure S5. Related to Figure 5.

A



B

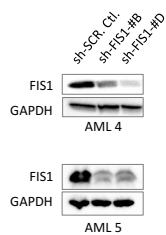


Figure S5. Related to Figure 5. Loss of FIS1 induces cell cycle arrest in AML

(A) GSEA enrichment plots showing loss of FIS1 in MOLM-13 cells (3 technical replicates) results in down-regulation of 3 cell cycle-related gene sets from the GSEA Reactome collection. “sh-FIS1” represents sh-FIS1-#B and sh-FIS1-#D together. (B) WB images showing knock-down efficiency of FIS1 in primary AML 4 and 5.

Figure S6. Related to Figure 6.

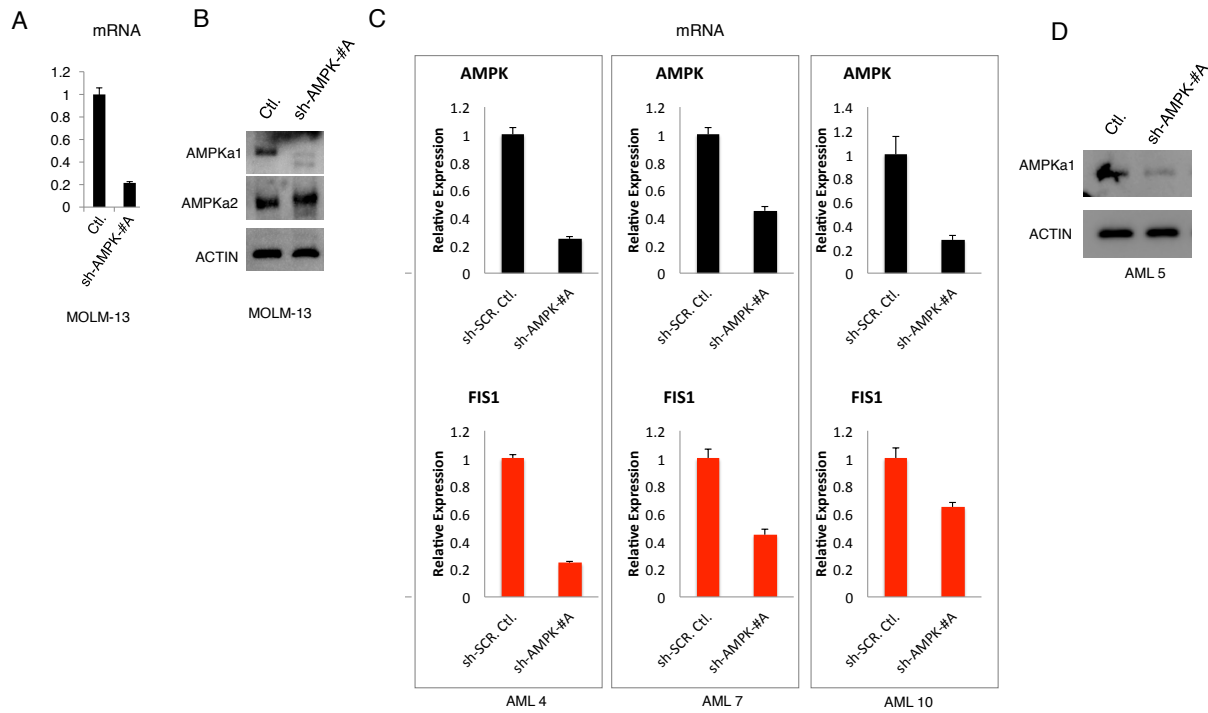


Figure S6. Related to Figure 6. AMPK affects FIS1 expression at transcriptional level

(A) qPCR results showing knock-down efficiency of shAMPK in MOLM-13. (B) WB images showing knock-down efficiency of shAMPK in MOLM-13. AMPKα2 was used as a control to demonstrate that the knock-down is specific to AMPKα1. Actin is probed as loading control. (C) qPCR results showing knock-down efficiency of shAMPK in primary AML and their impact on the FIS1 transcription. (D) WB images showing knock-down efficiency of shAMPK in primary AML 5. Related to Figure 6H.

Figure S7. Related to STAR METHODS: CRISPR/Cas9

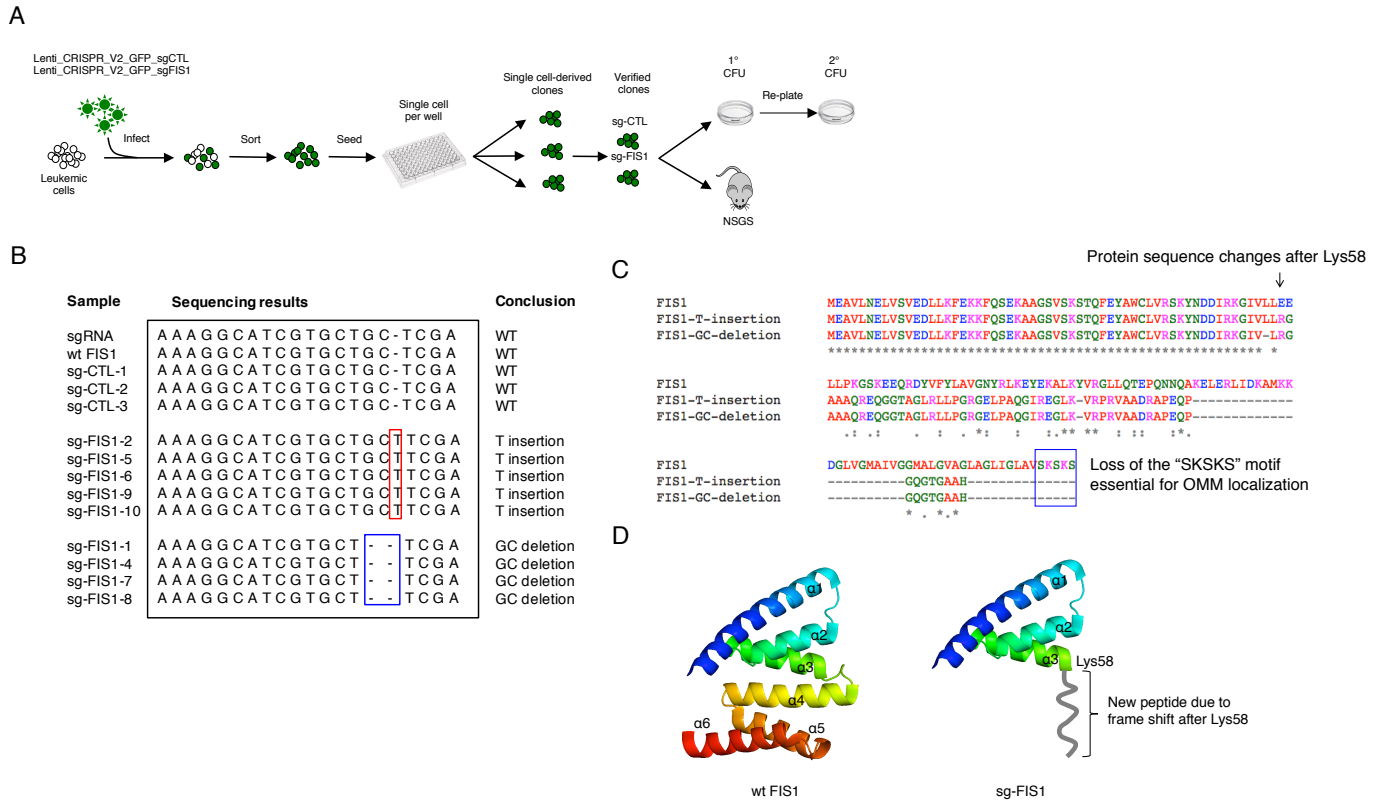


Figure S7. Related to STAR METHODS: CRISPR/Cas9. Design and verification of CRISPR/Cas9-mediated FIS1 disruption

(A) A schematic diagram showing generation of sg-CTL and sg-FIS1 clones and subsequent colony-forming and xenograft studies. **(B)** DNA sequencing results showing successful editing of wild type FIS1 allele to heterozygous FIS1 alleles containing T-insertion and GC-deletion. **(C)** Predicted protein sequences coded by wild type, T-insertion and GC-deletion FIS1 alleles. Both T-insertion and GC-deletion alleles result in new peptides due to frame shift after Lys58 and loss of the "SKSKS" motif essential for outer mitochondrial membrane localization. **(D)** Crystal structure of wild type FIS1 (PDB: 1nzn) and putative structure of sg-FIS1 (Assume structures of $\alpha 1$ - $\alpha 3$ helices are unchanged).